Volume 3
Number 6
November 2025
Pages 1395-1650

RSC Applied Polymers

rsc.li/RSCApplPolym

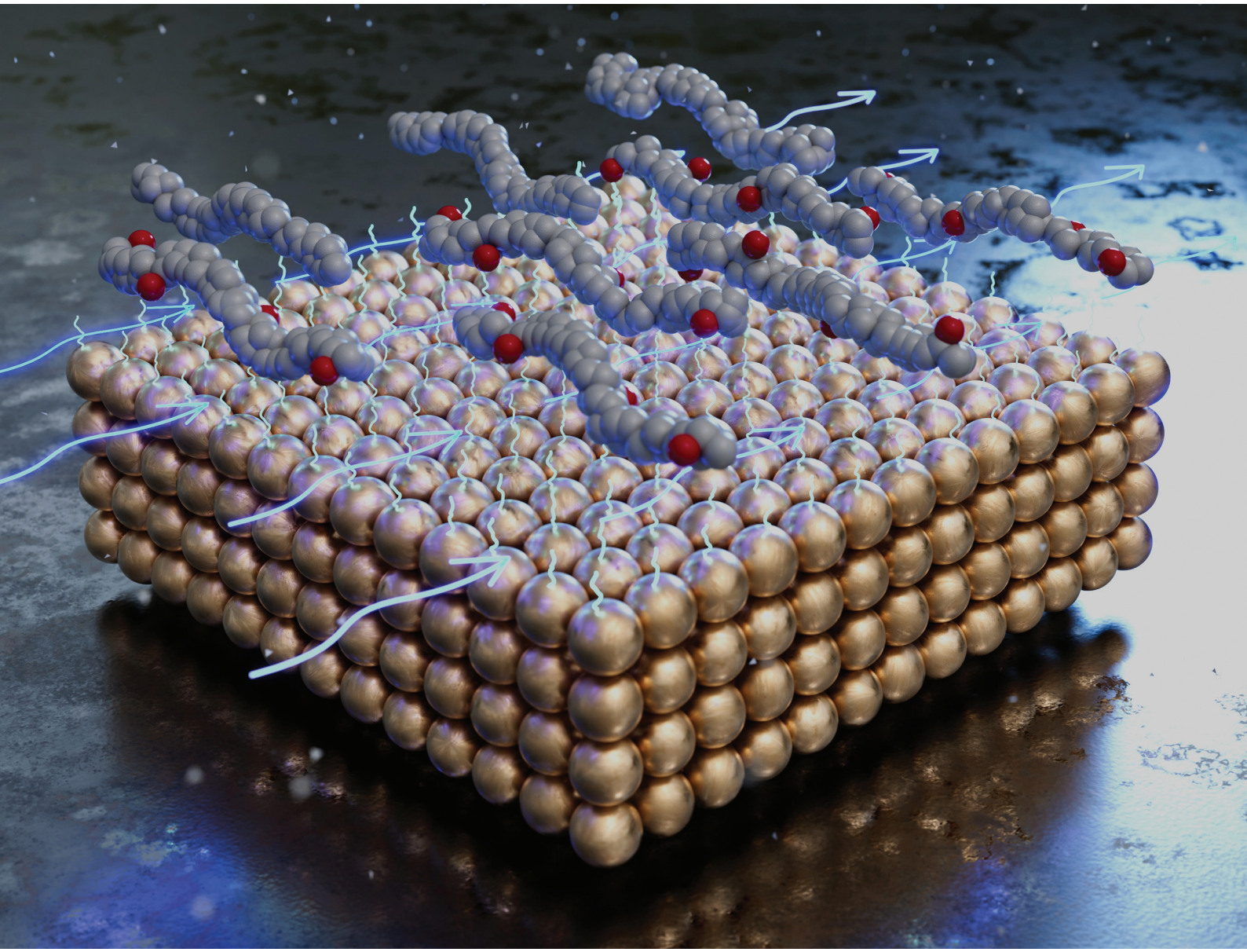

ISSN 2755-371X

ROYAL SOCIETY OF CHEMISTRY

PAPER
Shudipto Konika Dishari *et al.*
Interface-driven enhancement of Nafion thin-film conductivity *via* controlled aminothiol modification

RSC Applied Polymers

PAPER

View Article Online
View Journal | View Issue

Cite this: *RSC Appl. Polym.*, 2025, **3**, 1459

Interface-driven enhancement of Nafion thin-film conductivity *via* controlled aminothiol modification

Karen Acurio-Cerda,†[a] Oghenetega Allen Obewhere,†[a] Golam Azom,[b] Revati Kumar[b] and Shudipto Konika Dishari*[a]

The performance of electrochemical devices is critically influenced by the interfacial confinement of ionomer chains at the catalyst interface. In sub-μm-thick ionomer films at the catalyst interface, confinement of water and ionomer chains limits proton conductivity, hindering electrochemical reactions at the cathode and compromising fuel cell performance. Here, we investigated the effect of interfacial engineering on Nafion thin-film conductivity by covalently modifying gold (Au) electrodes with cysteamine (Cys), an aminothiol linker. Nafion films (~60 nm thick) spin-coated on Cys-modified Au exhibited up to 4-fold increase in in-plane proton conductivity (σ_{IP}) at 85% RH compared to films on bare Au, with insignificant changes in water uptake. Molecular dynamics (MD) simulations revealed that the Cys modification of Au induced a more surface-parallel orientation of the Nafion backbone near the substrate. This promoted highly ordered $-SO_3H$ groups and in-plane proton-conducting pathways while slightly lifting Nafion chains away from the hard wall-like Au surface. Attaching to the $-NH_2$ terminal of Cys, but hanging slightly up from Au, rendered a milder confinement to Nafion chains and surrounding water molecules. Consequently, the in-plane self-diffusion coefficients of water and hydronium ions increased, and the storage modulus of the films decreased, supporting more water-ionomer mobility and a milder confinement. While the more surface-parallel nature of ionomer chains with lower confinement on Cys improved in-plane proton conductivity of Nafion films, the out-of-plane conductivity did not change significantly for the same reason. These findings demonstrated the importance of controlling interfacial chemistry and linker design to gain control over ionomer chain orientation, confinement, and directional ionic conductivity, offering a promising strategy to enhance ion transport in thin ionomer films for next-generation electrodes and electrochemical devices.

Received 3rd August 2025,
Accepted 14th October 2025

DOI: 10.1039/d5lp00245a

rsc.li/rscapplpolym

Introduction

Electrochemical cells are at the core of clean energy technologies. Their performance, however, is often limited by ion and gas transport through the catalyst binder, an ultrathin ionomer layer that binds catalyst particles to electrode surfaces. In proton exchange membrane fuel cell (PEMFC) cathodes, for instance, sluggish ion transport at the ionomer–catalyst interface hinders the oxygen reduction reaction (ORR). Sub-μm-thick ionomer films like Nafion, when deposited on electrodes, exhibit proton conductivity 1–2 orders of magnitude lower than their bulk, free-standing membrane counterparts (typically tens of μm thick).[1–4] This reduced conductivity delays proton delivery to catalyst active sites, compromising ORR kinetics, power density, and overall device efficiency. This challenge underscores the need for focused design strategies targeting electrodes and ionomer-electrode interfaces. However, historically, research emphasized bulk membrane design where interfacial effects are minimal. Only recently has attention shifted to the behavior of ionomers under thin-film confinement, where ionomer-substrate interactions become dominant.

Geometric and interfacial confinements are primarily held responsible for the weak proton conductivity in thin ionomer films. As the film thickness approaches only a few times the ionomer's radius of gyration, polymer chain mobility[5,6] and diffusion[7] become increasingly restricted, a phenomenon known as geometric confinement. Interfacial confinement, on the other hand, arises from strong interactions among water molecules, the ionomer's sulfonic acid groups ($-SO_3H$), and the substrate, further constraining chain dynamics and disrupting the nanoscale phase separation necessary for efficient proton conduction.[5,6,8–16]

[a]*Department of Chemical and Biomolecular Engineering, University of Nebraska-Lincoln, Lincoln, Nebraska 68588, USA. E-mail: sdishari2@nebraska.edu*
[b]*Department of Chemistry, Louisiana State University 70803, USA*
† These authors contributed equally.

Perfluorosulfonic acid-based ionomer, Nafion, conducts protons through hydrated channels formed by $-SO_3H$-containing side chains and water molecules.[17–23] While $-SO_3H$ and H_2O naturally interact to form these conductive domains, they also strongly interact with substrates in Nafion thin films.[3,5,6,10–12,14–16,22,24–29] For example, a silica-based substrate with a native oxide layer can undergo interfacial interaction with water and $-SO_3H$ groups of ionomers *via* H-bonding.[3,5,6,9] Experimental and computational efforts consistently indicate that as Nafion film thickness approaches the polymer's radius of gyration or the length of the longer axis of self-assembled chain bundles in dispersion, the Nafion backbones can be compelled to align parallel to the substrate.[25,30–32] Kreuer *et al.*[23] simulated planar polymer-water sheets that fit well with experimental GISAXS data, indicating near-surface-parallel chain orientation of Nafion in thin films. Birefringence measurements,[10,25] ionomer peak analysis as a function of azimuthal angle (2D GISAXS),[33] and neutron reflectometry (NR)[34–37] further confirmed surface-parallel alignment of Nafion chains in sub-micron thick films, especially when film thickness drops below 100 nm.

This surface-parallel backbone orientation immediately next to the substrate naturally forces the side chains of Nafion to extend perpendicularly toward the substrate and makes its $-SO_3H$ groups interact more with the substrate. The water molecules accumulating next to the substrate[34,38] also participate in this interactive process, together causing ionomer chain pinning to the substrate. This observation extends beyond oxide substrates to metallic ones (Au, Pt), having close relevance in electrochemical studies and practical applications. Both Au and Pt are hydrophilic,[3,10,39] making them interactive with $-SO_3H$ groups.[26,27,40] Birefringence studies,[25] indicated surface-parallel orientation of Nafion backbones on these metals, while DFT calculations predicted ordered sulfonate layers on Pt.[41] Interactions between sulfonate groups and metal surfaces (both Au, Pt)[26,40] and ionomer chain adsorption[42] have been reported *via* sum frequency generation spectroscopy,[26] surface enhanced Raman spectroscopy,[40] electrochemical QCM and AFM imaging.[42]

If severe chain pinning happens near the substrate, the water-ionomer chains near the substrate should lose mobility, fail to spontaneously phase segregate, and show weak proton conduction near the substrate. This is exactly what we observed in depth-specific proton conduction profiles of Nafion films, obtained *via* confocal laser scanning microscopy (CLSM) imaging.[2] In Nafion films on glass substrates, up to half the film thickness near the substrate exhibits extremely weak proton conduction, which gradually improves toward the air interface.[2] Even under humidified conditions, when water accumulates near the substrate (as per NR[34,38]), this near-substrate region remains poorly conductive. Importantly, the interfacial water-ionomer interaction was found to stiffen ionomer films,[5,6] and the widths of the stiffened and low-proton-conducting zones were similar in Nafion films.[2] These demonstrate that ionomer chain pinning at the ionomer-electrode interface significantly impairs interfacial proton conduction in Nafion thin films. Such adsorption of $-SO_3H$ groups on the Pt surface not only weakens proton conduction but also blocks O_2 from reaching Pt catalyst active sites, impeding ORR under fuel cell operating conditions.[43] It is thus critical to optimize interfacial chemistry to alleviate interfacial chain pinning and boost thin-film proton conductivity and ORR activity.

By far, strategies to modify electrode-ionomer interfaces, include tailoring catalyst[37,44,45] and carbon support[46] structure and chemistry, altering substrate hydrophilicity[45,47–49] or zeta potential,[45] doping substrate with atoms (like N),[50–52] or incorporating/immobilizing molecules, such as ionic liquids (ILs),[49,53–56] IL-based block copolymers,[57–59] strategically designed ionomers for interconnected ion channels,[1,9,60,61] or engineered peptides[62–64] near electrodes. Structure and chemical makeup of catalysts[37,44,45] and carbon supports[46] have influenced catalyst activity, agglomeration, coverage, and stability, water-ionomer distribution, and proton and gas transport, thereby. IL-containing sulfonated block copolymers[57] or IL-modified catalyst pores[65] reduced Nafion coverage of Pt, which improved membrane electrode assembly (MEA)-level performance of PEMFCs. Certain ionomers were able to reduce chain crowding near the substrate interface, causing reduced chain pinning and improved proton conduction near the substrate interface as well as across the film.[60,61] Simulations also showed that, as opposed to staying in contact with Pt, if the $-SO_3H$ groups are slightly distant from the Pt (at the edge of Helmholtz plane), it can alleviate the blocking effect on ORR.[43]

While these findings strongly suggested weakening $-SO_3H/-SO_3^-$ adsorption on substrate as a key to improving ion conductivity in confined ionomer films and ORR activity in catalyst layers, it is still not clear which interfacial physical and chemical makeup is optimal to achieve so. Our previous work[10] attempted to address this gap by engineering SiO_2 substrates and Au electrodes with 3-aminopropyltriethoxysilane (APTES) and understanding its impact on thin film proton conductivity and other properties. APTES introduced a spiderweb-like barrier near the substrate, disrupting chain alignment and reducing surface pinning of Nafion. This was confirmed by decreased fluorine and sulfur signals near the substrate (*via* SEM-EDX), reduced film stiffening, and enhanced through-thickness proton conduction.[10] CLSM imaging further showed that APTES narrowed down the low-conductivity region next to the substrate and improved the proton conduction across Nafion films.[10] These findings suggested that a physical, small obstacle next to the substrate can go a long way by reducing chain pinning, chain confinement, and improving proton conduction behavior at the ionomer-electrode interface as well as across the film. Having said that, a big role will be played in these processes by the nature and length of the linker, but a systematic understanding of their influence has a long way to go.

To address these needs, this work explored the use of cysteamine (Cys) as a covalent linker on Au electrodes to engineer the ionomer-electrode interface (Fig. 1). Cys features a short ethyl side chain with terminal amino ($-NH_2$) and thiol ($-SH$) groups, enabling strong Au–thiol bonding and surface

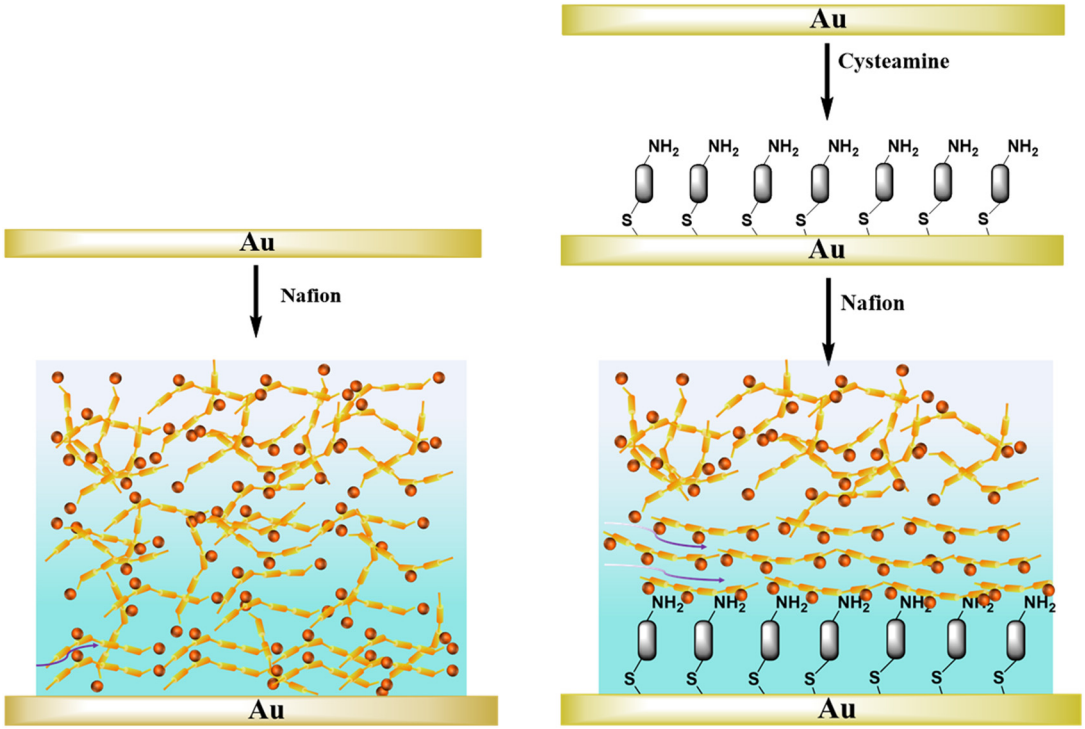

Fig. 1 Schematic illustrating (left) a Nafion film on bare Au, (right) Cys modification of the Au substrate/electrode followed by Nafion thin-film deposition. The perfluorinated backbones of Nafion chains in the films are represented by orange–yellow chains, while the red balls represent terminal sulfonic acid ($-SO_3H$) groups on the side chains appended to Nafion backbones.

functionalization without harsh treatments. Au is widely used for electrochemical characterization, and since Pt, the practical electrode material, also binds thiols,[66–68] insights gained here on the role of Cys modification on thin-film ion conduction behavior can translate to real device systems. Compared to APTES, forming a relatively thick (~9–12 nm) spiderweb-like structure while making Nafion chains less anchored to the substrate, Cys forms a compact, thinner (~0.7 nm), and more uniform monolayer next to the electrode that spatially organizes Nafion chains slightly away from the substrate, but in a more organized manner while minimizing direct ionomer-electrode interaction. This study aimed to understand how tailoring Au electrodes with Cys influences interfacial Nafion chain pinning, orientation, distribution, and ultimately proton conduction and water self-diffusion in confined thin-film environments. We combined experimental and computational approaches to reveal these interfacial processes caused by the Cys-based interfacial engineering, demonstrating an increase in in-plane proton conductivity of Nafion thin films.

Materials and methods

Materials

A 20 wt% Nafion solution (EW ~ 1100, IEC 0.909 meq g^{-1}) and cysteamine (Cys) were purchased from Millipore Sigma (Milwaukee, WI). Ethanol (anhydrous, denatured) was obtained from Decon Labs, Inc. (King of Prussia, PA). Silicon wafers coated with native silicon dioxide (SiO_2) (thickness of native oxide layer ~1.72–1.79 nm) were purchased from Wafer Pro (San Jose, CA). Au interdigitated electrodes (IDEs), used for in-plane proton conductivity measurements, were obtained from Revtek Inc. (Torrance, CA). Au-coated crystals (5 MHz, Ti/Au/Ti/, polished, 25.4 mm (1 inch) diameter) for quartz crystal microbalance (QCM) measurements were purchased from Inficon (Syracuse, NY).

Sample preparation

Au deposition on silicon wafers *via* magnetron sputtering. Titanium/gold (Ti/Au) multilayer films were deposited on single-sided polished silicon (100) wafers using a magnetron sputtering system (AJA International, Inc.). The deposition was conducted at a low Ar pressure of 5 mTorr. The system also features a sample load-lock to minimize exposure of the main chamber to atmospheric contaminants. Substrates were mounted face-down on holders attached to a rotating propeller located along the central axis of the main deposition chamber. The propeller rotated at approximately 45 Hz to ensure uniform film coverage. Sputtering rates were controlled by adjusting the sputtering power while maintaining the constant Ar pressure. The substrate-to-target distance and gun tilt were typically set to 30 mm and 2.5 inches, respectively, as indicated by the system dials. For Au deposition, a DC power supply was used with a power setting of 75 W, yielding a deposition rate of approximately 0.97 Å s^{-1}. For Ti, a separate DC source was

operated at 120 W, with a deposition rate of 0.39 Å s^{-1}. These sputtering conditions yielded a ~10 nm-thick Ti-adhesion layer, followed by a 50 nm-thick Au layer on top. These Au-coated Si-wafers were then used for subsequent Cys modification, Nafion film coating, and film characterization using X-ray photoelectron spectroscopy (XPS), scanning electron microscopy with energy-dispersive X-ray spectroscopy (SEM-EDX), ellipsometry, contact resonance atomic force microscopy (CR-AFM), and water contact angle measurements.

Cysteamine (Cys) self-assembly on Au-substrates. Au substrates (Au-coated silicon wafers, IDEs, QCM crystals) were modified with 10 mM Cys in a light-protected environment for 6 h, following previous reports.[69–72] Briefly, the modification process involved cleaning the Au substrates with acetone and ethanol, followed by air-drying and treatment with UV-ozone for 20 min. The cleaned Au substrates were immersed in a solution of 10 mM Cys in ethanol in glass vials. This enables string interaction between thiol (–SH) groups of Cys and Au, and the Au–S formation leads to immobilization of Cys on the Au surface. The entire modification process was conducted under dark conditions for 6 h. This protocol was designed to ensure a controlled and light-protected environment throughout the Cys modification process, aiming to achieve a consistent and reproducible modification of the Au surface. After 6 h incubation, substrates were carefully removed, rinsed thoroughly with ethanol to eliminate any unbound Cys, and subsequently dried using N_2. The samples were stored in a desiccated chamber for further ionomer deposition and/or analysis. The Cys immobilization on Au was verified *via* X-ray photoelectron spectroscopy (XPS), scanning electron microscopy with energy-dispersive X-ray spectroscopy (SEM-EDX), QCM, and ellipsometry measurements.

Ionomer thin film deposition. To produce Nafion thin films on unmodified and Cys-modified Au, a 20 wt% Nafion stock solution was diluted with ethanol, then vortexed for 1 min, and ultrasonicated for 15 min. This yielded 1–5 wt% Nafion solutions, which were spin-coated at 3000 rpm for 40 s on Au and Cys–Au substrates to get Nafion films with a thickness ranging between 15–120 nm. Before spin-coating, all the substrates were cleaned with ethanol and UV-Ozone-treated for 20 min. The Nafion films spin-coated on Au and Cys–Au were then dried for 3 h at 42 °C, annealed at 100 °C for 7 h, and cooled down to r.t. overnight inside a vacuum oven (Model #1415, VWR, Radnor, PA).

SEM-EDX measurements. Elemental mapping to confirm Cys functionalization on Au was done using SEM-EDX. For this imaging, FEI Helios 660 NanoLab field emission SEM with EDX detector was used with an acceleration voltage of 20 kV in immersion mode. EDAX TEAM software was utilized for chemical mapping and elemental data acquisition. To enhance image contrast and protect the samples from electron beam damage, an Au layer was coated on top of the substrates using a Cressington Au sputter coater. All measurements were conducted under high vacuum conditions.

Water contact angle (WCA) measurements. WCAs of bare Au, Cys-modified Au substrates, and Nafion films on those substrates were determined using a Ramé-Hart Model 590 F4 Series Goniometer and Tensiometer. A 5 μL water droplet was applied using the sessile drop method, and a digital photograph was taken for precise WCA measurement.

In-plane proton conductivity measurements. To determine thin-film impedance and proton conductivity of Nafion films on Au and Cys–Au, Solartron 1260a Impedance/Gain-Phase analyzer (Solartron Analytical, Leicester, England) was used with a 2-probe technique as reported earlier.[1,10,73] For in-plane proton conductivity measurements using electrochemical impedance spectroscopy (EIS), Au interdigitated electrodes (IDEs) were fabricated on silicon wafers (110), featuring a thermally grown SiO_2 layer (200 nm) as an electrical insulator. Each IDE consisted of 150 gold teeth, each being 8 μm wide, spaced 40 μm apart, with an overlapping length of 4 mm. The IDEs were modified with Cys and spin-coated with Nafion as mentioned earlier in the sample preparation section. To ensure optimal cleanliness of the contact pads, the segments of the films covering them were removed using a small brush saturated with ethanol. Subsequently, the contact pads were left to air-dry. Following this, the Nafion thin film-coated and bare/Cys-modified interdigitated electrodes (IDEs) were promptly placed on a temperature stage set at 22 °C inside an environmental chamber. The Au tips of the probes were positioned carefully onto the IDE contact pads. The relative humidity (% RH) of the environmental chamber was controlled using silica gel for ~0–5% RH, K-acetate for ~25% RH, K_2CO_3 for ~50% RH, NaCl for ~75% RH, and Na_2SO_4 for ~90% RH. By passing dry air (0.5 ft^3 h^{-1}–235 cm^3 min^{-1}) through a bottle/container containing the silica gel or saturated salt solution (immersed in a water bath at 23 °C), air with a specific % RH was generated, which was then passed through the environmental chamber. A humidity sensor was strategically placed at the chamber outlet to continually monitor and ensure the attainment and maintenance of the targeted % RH level within the chamber. At each humidity condition, the samples were stabilized for 1 h inside the environmental chamber prior to EIS measurement. Within this 1 h period, the impedance of the samples was measured periodically (at about every 14 min, from 1–10 kHz frequency range) to ensure sample stability at a specific % RH condition. Once stabilized, the impedance response of the Nafion film was recorded over a frequency range from 10 MHz to 1 Hz at an AC potential of 100 mV (choice of AC voltage is discussed in the discussion of Fig. S5a). The in-plane impedance data were analyzed using ZView software from Scribner Associates (Southern Pines, NC), which employed an appropriate equivalent circuit model (Fig. S5b) to fit the impedance spectra (Fig. 5a–c and S5c) and determine the film resistance (R_f) in the in-plane direction. The selection of components for the equivalent circuit model and the fitting process were based on our previous work.[1,10] Subsequently, the values of film resistance (R_f), film thickness (d_{film}), and the parameters of the interdigitated electrodes (IDEs)—including the spacing between teeth (S_{teeth}), overlapping length of each tooth (l), and number of teeth (N)—were

utilized in eqn (1) to calculate the in-plane proton conductivity (σ_{IP}) of the films.

$$\sigma_{IP} = \frac{1}{R_f} \frac{S_{teeth}}{l(N-1)d_{film}} \quad (1)$$

Please see the SI for representative Bode plots (Fig. S6a and b), residual plots (Fig. S6c–f), and χ^2 values (obtained upon fitting the impedance data, Table S3).

The protocols for measuring and fitting out-of-plane impedance data to obtain out-of-plane proton conductivity (σ_{OP}) are also discussed in the SI (Fig. S7 and eqn (S3)).

Water uptake measurement. To measure the effect of Cys on water sorption within Nafion films, Au-coated quartz crystal microbalance (QCM) crystals were modified first with Cys (as described earlier), then Nafion films were deposited on top. Water uptake of Nafion films on unmodified and Cys-modified Au crystals was measured using a QCM system (Stanford Research Systems (Sunnyvale, CA)). Nafion film-coated Au crystals were placed on a crystal holder within a custom-designed plastic humidity chamber. The humidity inside the chamber was maintained using appropriate saturated salt solutions. All QCL samples were equilibrated at each % RH for at least 1 h.

The dry mass of Nafion film on a QCM crystal ($m_{\text{dry Nafion film}}$) was determined at ~5% RH by analyzing the corresponding frequency change ($\Delta f = f_{\text{dry Nafion film on crystal}} - f_{\text{bare crystal}}$).[7,74] To calculate water uptake or hydration number (λ_w) of Nafion films, the Sauerbrey equation was used. The choice of the Sauerbrey equation is appropriate for the film thickness range (~15–100 nm thick) we studied, since within this thickness range, dissipative loss remains insignificant.[75,76] In the Sauerbrey equation, the bare crystal frequency was used as ~5 MHz, active crystal area (A) as 1.27 cm^2, density of quartz crystal (ρ_q) as 2.648 g cm^{-3}, and shear modulus of quartz (μ_q) as 2.947×10^{11} g cm^{-1} s^{-1}.[2,77] The total mass of water sorbed by Nafion films ($m_{\text{water sorbed}}$) at each % RH was obtained by analyzing the corresponding frequency change ($\Delta f = f_{\text{wet Nafion film on crystal}} - f_{\text{dry Nafion film on crystal}}$). The water mass sorption by each ionomer film was corrected further by subtracting the water absorption by bare QCM crystals at the same % RH, following the standardized protocol reported earlier.[11,77–79] This corrected mass of water sorbed by a Nafion film at certain % RH ($m_{\text{water sorbed, corrected}}$) and dry mass of Nafion film ($m_{\text{dry Nafion film}}$) were used to obtain hydration number (λ_w), moles of water per mole of sulfonic acid, at certain % RH using eqn (2):

$$\lambda_W = \left(\frac{m_{\text{water sorbed, corrected}}}{M_{H_2O}}\right)\left(\frac{1000}{m_{\text{dry Nafion film}} \times \text{IEC}}\right) \quad (2)$$

Here, M_{H_2O} is the molecular mass of water, and IEC is the ion-exchange capacity of Nafion.

Results and discussion

Au surface modification

To investigate the effect of interfacial engineering, we created a self-assembled layer of Cysteamine (Cys) on Au prior to spin-coating 15–100 nm thick Nafion films on top. A standard protocol was followed to immobilize Cys on Au *via* Au–thiol (–SH group of Cys) interactions, as detailed in the sample preparation section and illustrated in Fig. 1. Quartz crystal microbalance (QCM) measurements revealed that ~0.515 ± 0.033 μg of Cys attached to the active area of the Au-coated QCM crystals (1.27 cm^2) (Fig. S1), forming a ~1 ± 0.27 nm (10 ± 2.7 Å) thick chemisorbed layer of Cys on Au (from ellipsometry). This experimentally determined thickness of the Cys layer closely matched what was predicted by molecular dynamics (MD) simulations (~6.6 Å), and suggested the likelihood of the formation of a monolayer of Cys on Au, agreeing with the literature.[80,81]

Cys adsorption was further confirmed *via* elemental analysis using XPS (Fig. 2a–c) and chemical mapping using SEM-EDX (Fig. 2d–g). XPS analysis showed the emergence of N 1s and S 2p peaks after treatment with Cys, a molecule having both N (amine, $-NH_2$) and S (thiol, –SH) (Fig. 2a–c). In contrast, no N 1s and S 2p peak was observed for bare Au samples (Fig. 2a–c). Specifically, the S 2p peak at 162.1 eV (Fig. 2b) was attributed to the formation of S–Au bonds,[82] while a smaller secondary peak at 168 eV likely corresponded to oxidized sulfur species (sulfonates or sulfinates), commonly reported byproducts of Au-SH reactions.[82–84] Notably, our Cys immobilization protocol (6 h reaction under dark conditions) was optimized to minimize the formation of oxidized sulfur compounds, as indicated by the relatively low intensity of the 168 eV peak. The N 1s peak at 399.08 eV (Fig. 2c) further confirmed the presence of $-NH_2$ groups from immobilized Cys.[82] The corresponding elemental analysis showed an increase in both nitrogen and sulfur content upon Cys modification: N: 0% (bare Au) to 6.22% (Cys–Au); S: 0% (bare Au), 4.61% (Cys–Au) (Table S1).

The water contact angle measurements (Fig. 3a) indicated that Cys-modification increased the hydrophilicity of the Au surface (bare Au: 63°; Cys–Au: 46°). Birefringence of this Cys layer on Au was positive (Δn = +0.0018), indicating surface normal orientation of Cys linkers on Au. A similar surface-perpendicular orientation of Cys on Au was reported by others.[84,85] These results aligned with the anticipated orientation of Cys molecules: thiol (–SH) groups of Cys bind to the Au surface, leaving terminal $-NH_2$ groups exposed at the air interface. Subsequent deposition of Nafion films on both unmodified and Cys-modified Au resulted in similarly hydrophobic film-air interfaces, with minimal differences in water contact angles (Nafion on bare Au: 98°, Nafion on Cys–Au: 92°) (Fig. 3a). This suggested that the Cys modification impacted Nafion chains residing next to the substrate interface more than residing near the air interface. Having said that, the difference in hydrophilicity between Nafion-substrate and Nafion-air interfaces saw an increase upon Cys modification.

Based on AFM (Fig. S2), Cys modification reduced the roughness of the Au surface by one-third (1.56 nm (bare Au); 0.53 nm (Cys–Au)). This indicated that Cys modification created a smoother/flatter interface for Nafion chains to sit on the substrate. The increased substrate hydrophilicity and a

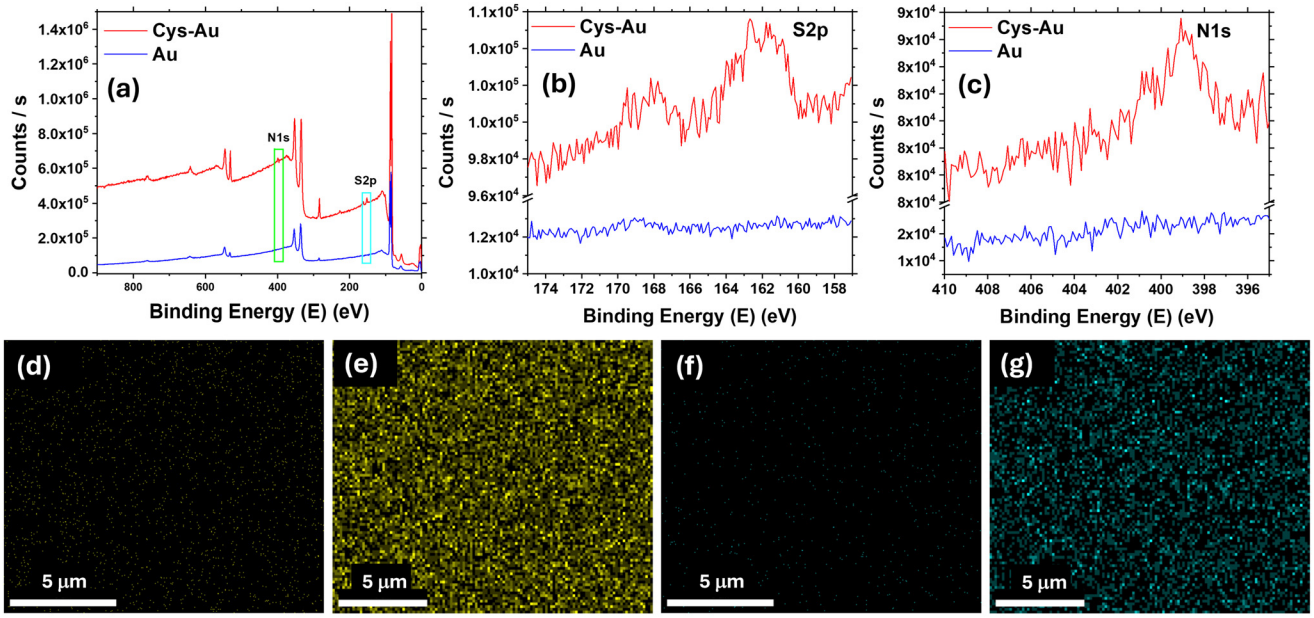

Fig. 2 (a–c) XPS (a) survey spectra, (b) S 2p and (c) N 1s spectra of bare Au (blue) and Cys on Au (Cys–Au, red) substrates. (d–g) SEM-EDX images showing the elemental mapping of sulfur: on Au (d) and Cys–Au (e); nitrogen: on Au (f) and (g) Cys–Au.

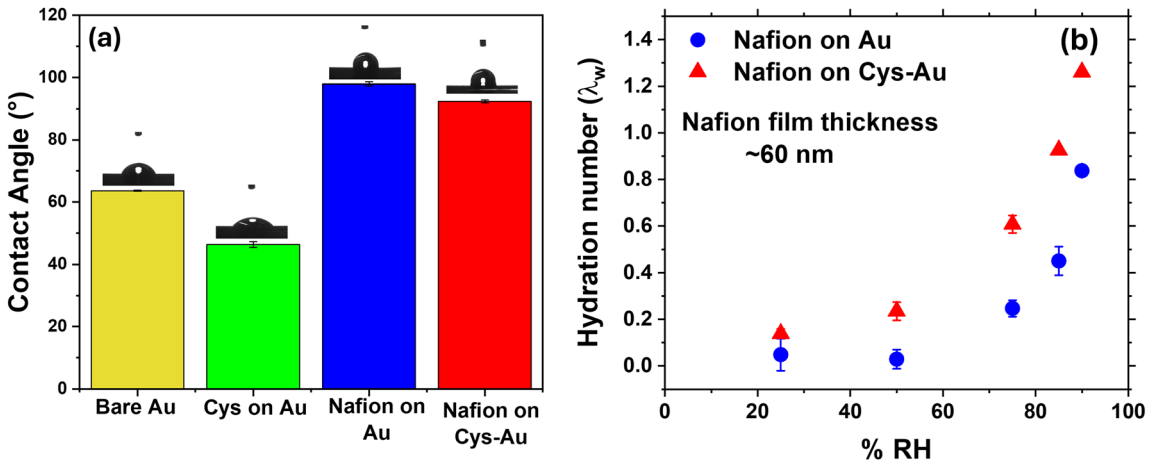

Fig. 3 (a) Water contact angle of bare Au (yellow), Cys-modified Au (green), 60 nm thick Nafion thin film spin-coated on Au (blue), and 60 nm thick Nafion thin film on Cys-modified Au (red). (b) Hydration number (λ_w = moles of H_2O/moles of SO_3H) as a function of % relative humidity (% RH) for ~60 nm thick Nafion films on unmodified (blue) and Cys-modified Au (red). Measurements were done in triplicate, and error bars were calculated based on standard deviations.

flatter, smoother Cys interface may favor parallel Nafion backbone orientation[86] immediately next to Cys, which may dictate the $-SO_3H$ groups of Nafion side chains to point toward Cys and interact with its $-NH_2$ groups. This experiment-based prediction agreed with findings from MD simulations (Fig. 4).

Fig. 4a and b show the probability distribution of $\cos\theta$ ($P(\cos\theta)$) for the first layer of Nafion on bare Au and Cys–Au, respectively, where θ is the angle between the Nafion bisector vector (V_{NB}) and surface normal vector (V_s) (Fig. S3). For instance, when the two segments of the Nafion backbone lie parallel to the substrate, the Nafion bisector lies in the plane of the substrate and forms a 90° angle with the surface normal, resulting in $\cos\theta = 0$. In contrast, the bisector aligns at 180° or 0° with the surface normal vector when the Nafion backbone fragments create a V-–shaped conformation oriented downward or upward, corresponding to $\cos\theta$ values of −1 and +1, respectively. As can be seen in Fig. 4a, Nafion chains in the first layer on bare Au exhibit a broad distribution of orientation, with $\cos\theta$ ranging between −0.25 and +0.75. In contrast, Fig. 4b showed a sharp, high-intensity peak with a maximum at $\cos\theta = 0.4$ with a shoulder near $\cos\theta = 0$ for the first layer of Nafion chains on Cys-modified Au. Also, the edge

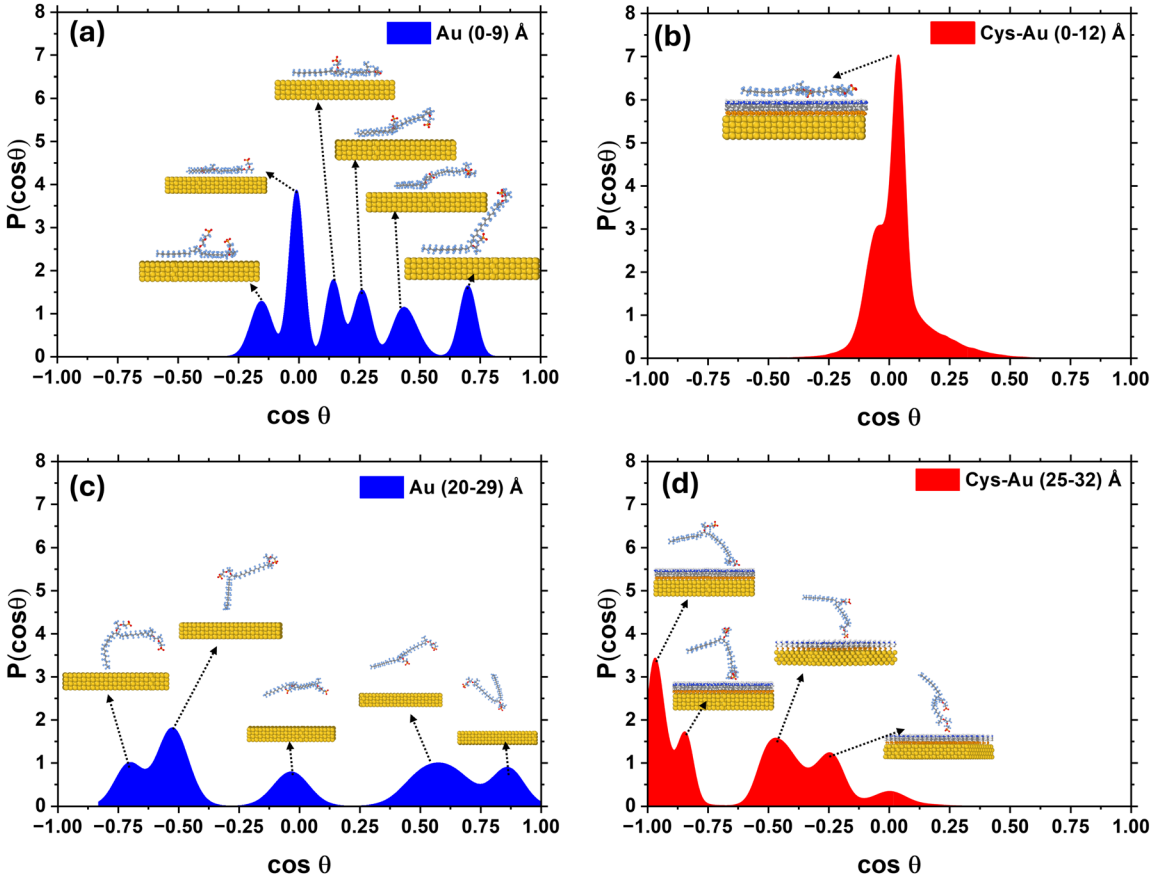

Fig. 4 MD simulations. (a and b) Probability distribution of cos θ ($P(\cos\theta)$) for the first layer of Nafion on (a) Au (considering 4 Å due to van der Waal forces and first Nafion layer ~5.4 Å thick) and (b) Cys-modified Au (considering the thickness of Cys layer as ~6.6 Å). (c and d) $P(\cos\theta)$ beyond the first layer of Nafion on (c) Au and Cys–Au (d). Representative snapshots are provided of the Nafion molecule orientation with respect to the Au surface for the different maxima in the distributions.

sulfonyl groups tend to point towards the Cys surface. The near-zero cos θ value indicates that Nafion backbones predominantly lie surface-parallel on top of Cys-terminated Au. These computational findings align with experimental observations (flat, smooth Cys surface from AFM roughness), suggesting that Nafion backbones adopt a more parallel orientation with higher order next to the substrate when deposited on Cys–Au compared to bare Au. It is important to highlight that the simulated Nafion film thickness (~3.4 nm) is notably smaller than the experimental range (~15–100 nm), and thus the results primarily reflect interfacial effects rather than bulk-like regions.

Previous works have shown that surface-parallel backbone orientation of ionomer chains could lead to chain pinning to substrate (confinement) and reduced proton conductivity. But interestingly, in this work, the highly ordered surface-parallel backbone orientations of Nafion chains on Cys–Au made a positive impact, enhancing in-plane proton conductivity (σ_{IP}) (unlike Nafion films on unmodified substrates). We measured σ_{IP} of annealed Nafion films (~15–100 nm thick) on unmodified Au and Cys-modified Au IDEs. Diameters of semicircles in Nyquist plots for σ_{IP} decreased as the Nafion film was deposited on Cys–Au (Fig. 5a–c). Since the decrease in semicircle diameter indicates a decrease in film resistance and an increase in film proton conductivity, the Nyquist plots indicated that Cys modification of the substrate interface can effectively improve in-plane proton conductivity (σ_{IP}) of Nafion in thin films. This improvement was consistently observed across the entire film thickness range we studied (Fig. 5d), with the deposition of a Cys layer beneath the Nafion film yielding up to a 4-fold increase in σ_{IP}. For instance, a ~65 nm thick Nafion film showed σ_{IP} of 27.6 mS cm^{-1} on Cys–Au, while it showed 7.5 mS cm^{-1} on bare Au IDEs at 85% RH (Fig. 5d). Even under low humidity conditions (except 20% RH), a 2–3-fold enhancement in σ_{IP} was observed when Nafion films were deposited on Cys–Au (Fig. 5e). The improved in-plane proton conductivity could be a combined outcome of reduced interfacial confinement effect (discussed later with more evidence) as well as Nafion side chains creating highly ordered ion-conduction pathways in the in-plane direction (*i.e.*, parallel to substrate). The thickness range investigated here is comparable to that of ionomer binder layers used in fuel cell electrodes, demonstrating the potential of interfacial engineering strategies to alleviate ion transport limitations in catalyst layers.

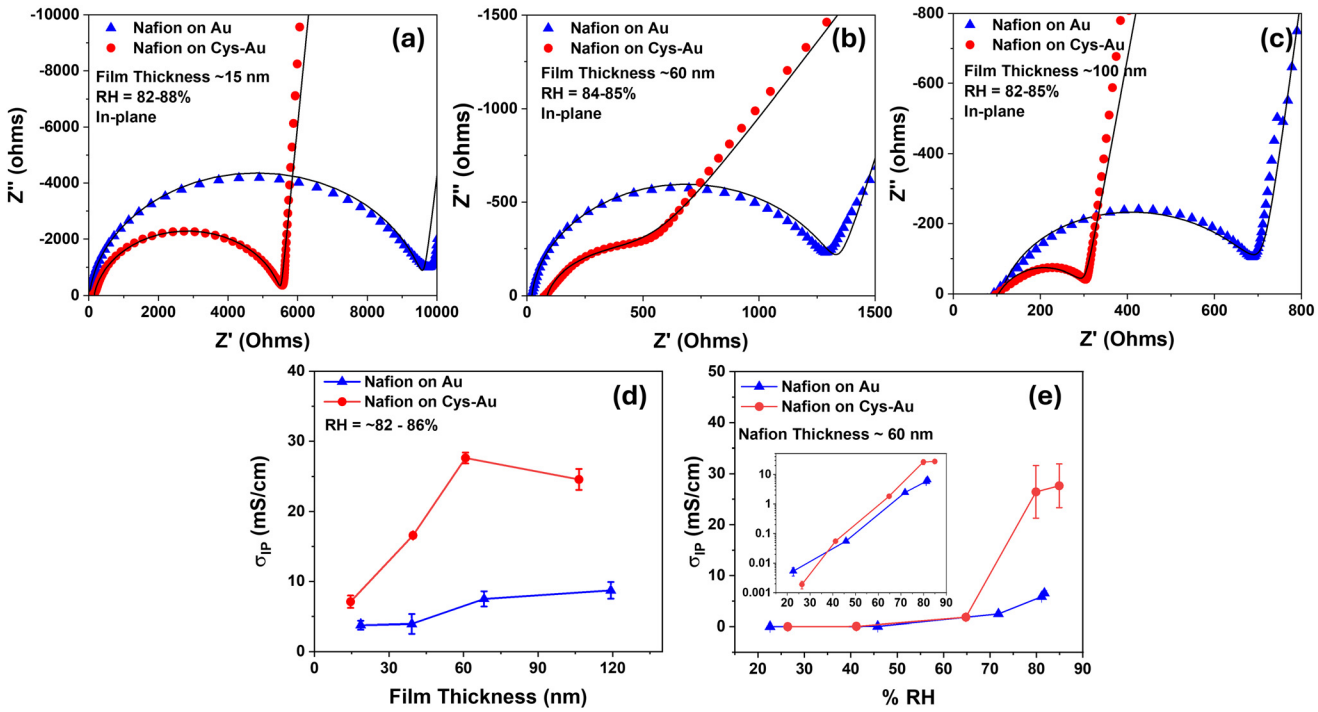

Fig. 5 In-plane Nyquist plots of (a) ~15 nm, (b) ~60 nm, and (c) ~100 nm thick Nafion films on unmodified and Cys-modified Au (Cys–Au) electrodes at ~85% RH. (d) In-plane proton conductivity (σ_{IP}) of Nafion films on unmodified and Cys–Au electrodes at ~85% RH as a function of film thickness. (e) σ_{IP} of ~60 nm thick Nafion films on Au and Cys–Au as a function of % RH. The equivalent circuit model used to obtain σ_{IP} values is shown in Fig. S5b in the SI. Measurements were done in triplicate (n = 3), and the results in Fig. 5d and e are presented as mean ± standard deviation (error bars).

To understand the contribution of Cys, we measured the conductivity of Cys-modified Au IDE (without a Nafion layer on top). The resistance of the Cys layer was very high: 8×10^7 ohms, which was about 5 orders of magnitude higher than that of Nafion films. This confirmed that Cys's intrinsic conductivity was very low and had a negligible contribution to the improvement of the Nafion film conductivity.

The hydration behavior, studied using QCM, showed that Nafion films on Cys–Au absorbed slightly more water than those on bare Au (Fig. 3b). However, such a small difference in water uptake (λ_w ~ 0.8 (Nafion on Au) *vs.* 1.2 (Nafion on Cys–Au)) should not account for the 4-fold improvement in proton conductivity (Fig. 5), suggesting a complex interplay of hydration with other factors, such as chain orientation within Nafion films, in modulating proton conductivity. In fact, based on experimental evidence and MD simulations, it can be inferred that the Cys layer was mainly responsible for internal change in Nafion chain distribution and organization next to the substrate (Fig. 4a and b) and within the film (Fig. 4c and d), causing improvement in σ_{IP} of Nafion thin films. The more surface-parallel orientation of the Nafion backbone induced by Cys–Au immediately next to it was discussed earlier. MD simulation also allowed us to predict the water (H_2O), hydronium (H_3O^+) ion, and Nafion chain distribution next to the substrate.

Fig. 6a and b show the normalized density distribution and probability of having hydronium ions (H_3O^+) and water (H_2O) (with representative snapshots in Fig. S4c and S4d, respectively), while Fig. 6c represents the probability of having Nafion chains as a function of z-distance from the Au surface (with representative snapshots in Fig. S4a and S4b). For Nafion films on bare Au, the density of H_3O^+ ions was consistently low across 45 Å thickness starting from the Au interface (Fig. 6a, blue). While Nafion film on bare Au did not exhibit any H_3O^+-rich region next to the substrate, a sharp increase in H_3O^+-ion density was observed at ~8 Å distance from Au when Nafion was deposited on Cys–Au (Fig. 6a, red). A similar spike in water (H_2O) density was observed at 9.3 Å distance from Au when Nafion was deposited on Cys–Au (Fig. 6b, red). This corresponded to a distance of ~2.7 Å from the Cys layer. Also, the peak intensity of the first water layer was almost double for the Cys-modified Au surface as compared to the neat Au surface (Fig. 6b). This observation indicated that water molecules preferentially reside in close proximity to the Cys–Nafion interface, rather than within the Cys layer.

In addition to forming this water-rich layer next to Cys, the starting depth of the Nafion chain population shifted up next to Cys when the Au surface was modified with Cys (Fig. 6c). The shifted molecular distribution of Nafion chains (*i.e.* next to Cys, not next to Au) can be rationalized *via* several findings: (i) as per MD simulations, the Cys layer is ~7 Å thick. (ii) As per QCM, area-specific density of Cys was 3.19×10^{15} molecules per cm^2, which was of the same order of magnitude of what is theoretically expected for a monolayer of Cys, assuming

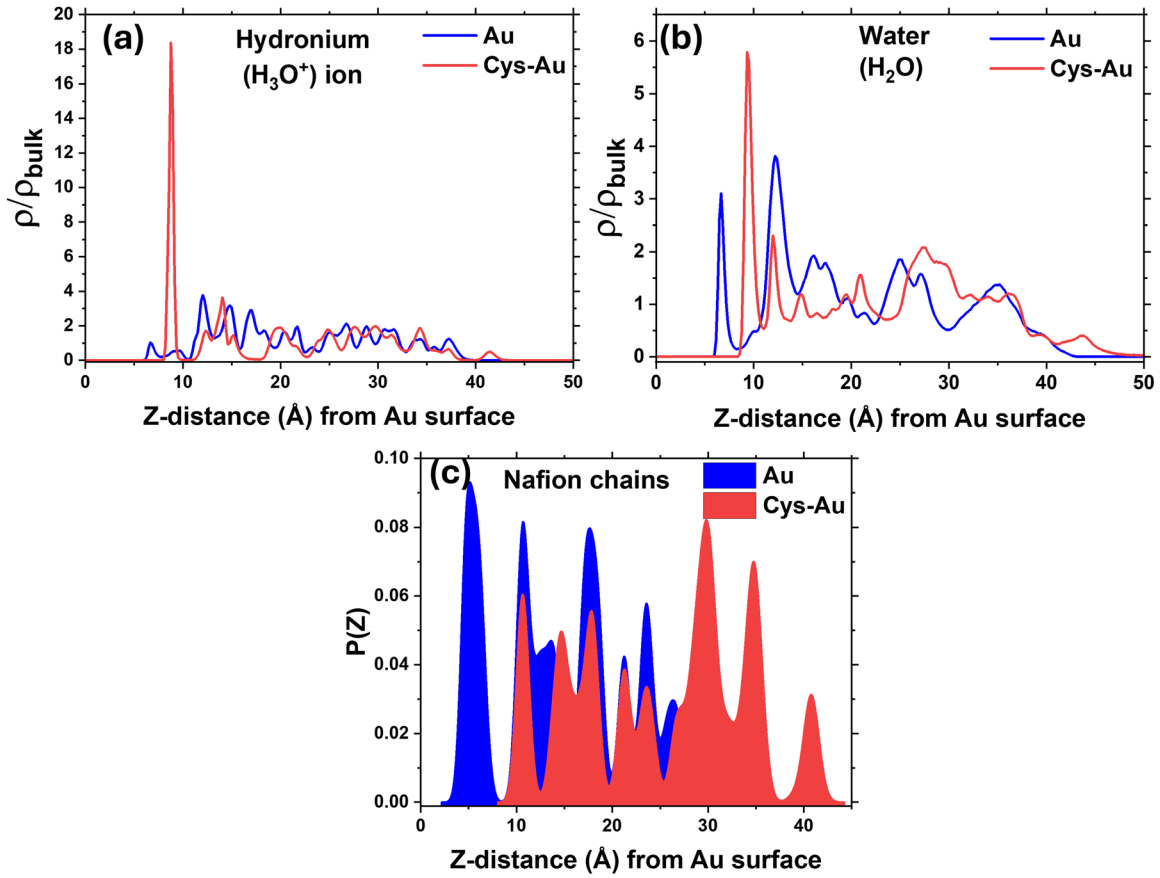

Fig. 6 Normalized density distribution of (a) hydronium (H_3O^+) ion and (b) water (H_2O) for Nafion on Au and Cys–Au. (c) Probability distribution of Nafion chains with the *z*-distance from the substrate.

each Au atom is attached to one Cys molecule (1.58×10^{15} molecules of Cys per cm^2). Thus, the dense Cys layer next to Au may have inhibited Nafion chain intercalation within Cys. The negligible density of H_3O^+ ion and water within the Cys layer, on the other hand, can be rationalized by the hydrophobic nature of the aliphatic linker in the mid-region of Cys molecules. While Cys's hydrophobic linker may have inhibited the water localization within the Cys layer, the terminal hydrophilic $-NH_2$ groups of Cys may have stimulated Nafion (with $-SO_3H$), water, and H_3O^+ ions sit on top of it, creating a water- and H_3O^+ ion-rich layer next to Cys. This aligns with prior neutron reflectometry-based observations[86] where hydrophilic and smooth surfaces create a more water-rich layer next to the substrate when hydrated. Having said that, the average hydration number (moles of water per moles of $-SO_3H$) for the entire film did not see much change due to Cys modification (Fig. 3b). This likely suggested that the water-rich layer next to the substrate may have sacrificed hydration in the upper part of the Nafion film (*i.e.*, adjacent to the air interface). This also suggested that the Cys-induced improvement in in-plane proton conductivity may predominantly be a localized effect. The orientational distribution, revealed from MD simulations, also supported that it is immediate next to Cys where chains are more parallel to substrate (beneficial for improving in-plane proton conductivity), but as we moved away from that position to up into the film (toward air interface), the Nafion chain orientation became more random with broad distribution of $\cos\theta$ values (Fig. 4d), just like what we observed at similar position in Nafion films on bare Au (Fig. 4c).

The improvement in in-plane proton conductivity (σ_{IP}) was also in complete agreement with the in-plane (H_3O^+) ion- and water (H_2O) self-diffusion coefficient ($D_{self,\ H_3O^+,\ IP}$ and $D_{self,\ H_2O,\ IP}$) in Nafion thin films. We observed about 4-fold increase in σ_{IP} (SI, Fig. 5d) as well as $D_{self,\ H_2O,\ IP}$ (4.3×10^{-9} m^2 s^{-1} (Nafion on Cys–Au) *vs.* 1.4×10^{-9} m^2 s^{-1} (Nafion on Au)) (Fig. 7a) and $D_{self,\ H_3O^+,\ IP}$ (5.57×10^{-13} m^2 s^{-1} (Nafion on Cys–Au) *vs.* 1.9×10^{-13} m^2 s^{-1} (Nafion on Au)) (Fig. 7b). As is known, self-diffusion coefficient of a species is correlated to its mobility by the equation: $D_{self} = \mu \times K_B \times T$, where μ is the mobility of the species, K_B is Boltzmann constant, and T is temperature. Thus, an increase in the water self-diffusion coefficient indicates an increase in water mobility.

Especially, the likelihood of increasing near-substrate proton conductivity (discussed in earlier section), likely points towards alleviated confining effects due to interfacial interactions. Although the $-NH_2$ groups on top of Cys–Au can still induce some H-bonding and electrostatic interaction-induced confinement, the Cys-modified surface may still be considered

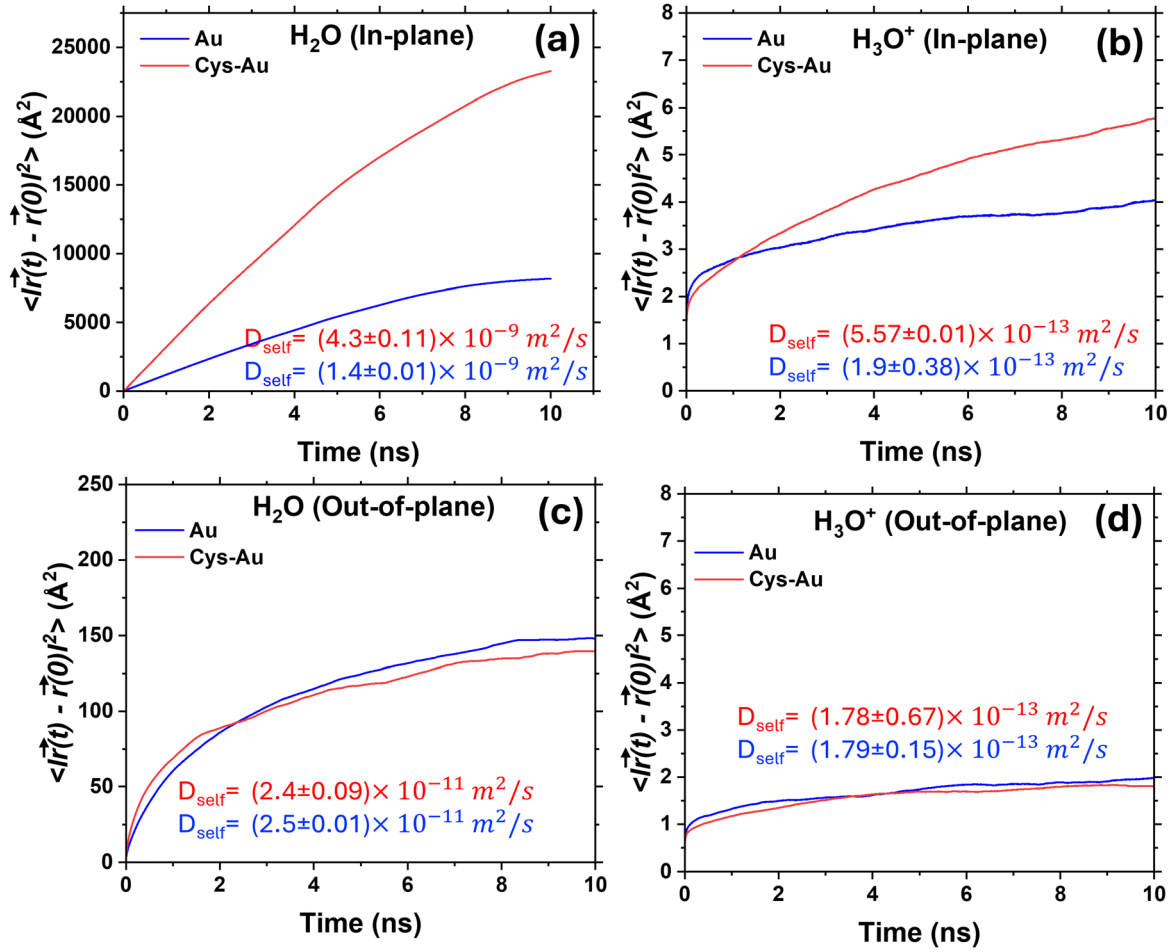

Fig. 7 Mean square displacement of water and hydronium (H_3O^+) ions in Nafion films on Au and Cys–Au: (a) water, in-plane; (b) H_3O^+ ions, in-plane; (c) water, out-of-plane; (d) H_3O^+ ions, out-of-plane. Corresponding self-diffusion coefficients (D_{self}) of species in a certain direction are shown in insets.

as a source of soft confinement for both water molecules and Nafion chains, whereas bare Au as a source of hard confinement. This is because Au creates a rigid, non-penetrable boundary (hard confinement) that restricts molecular movement only on one side (*i.e.* on top of Au surface). In contrast, Cys, being a little away from Au, provides water and Nafion chains multi-directional freedom to move around, even though they are anchored to Cys to some extent and hanging in there (soft confinement). It is like a fruit hanging from a tree *vs.* one lying on the ground. The hanging fruit can swing freely in all directions (*i.e.*, retains its dynamic freedom), while the fruit on the ground has its motion completely blocked on one side. Thus, despite some interfacial interactions, water may have a higher degree of rotational freedom, and Nafion chains may have higher segmental motion on top of Cys compared to on top of bare Au. Literature has shown this hard *vs.* soft confinement effect in terms of glass transition temperature, segmental dynamics, and structural relaxation.[87,88] This translational/rotational freedom (or mobility) favors proton transport.

Additionally, the storage modulus of Nafion films (Fig. 8) decreased when it was made on Cys-modified Au. This indi-

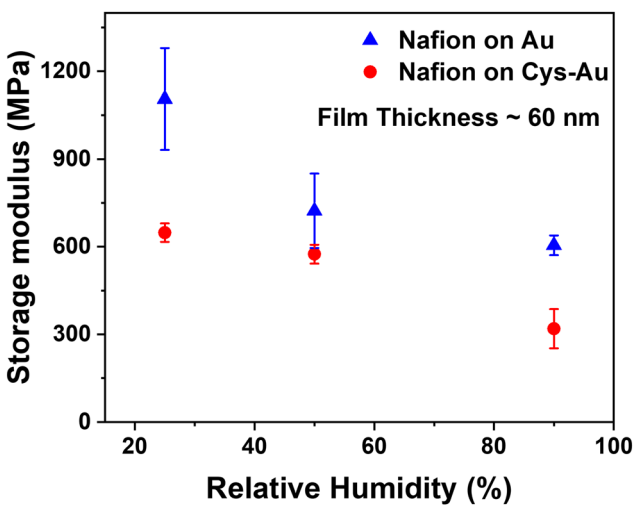

Fig. 8 Storage modulus of ~60 nm thick Nafion films on unmodified and Cys-modified Au at different % RH. Error bars are from the standard deviations of triplicate measurements.

cated that Cys modification allowed plasticization of Nafion film overall, which agreed with predicted faster water-ionomer chain dynamics owing to reduced confinement. This is in contrast with the typical response of Nafion films, which antiplasticized on affine substrates, but not in bulk membranes (free of interfacial effects).[5,6] This again presented a testament that if the interfacial effects are less, film stiffening will be less. Our prior observation in multiple cases also supported this connection, as we saw that when near-substrate $-SO_3H$ accumulation decreased, substrate pinning and storage modulus reduced.[10,60] Overall, a simultaneous increase in in-plane proton conductivity and in-plane water self-diffusion coefficient indicates that Cys immobilization next to the substrate likely alleviated the confining effect exerted by the substrate on water and protons in Nafion film, leading to an increase in in-plane proton conductivity.

While we achieved an improvement in in-plane proton conductivity (σ_{IP}) in the presence of Cys, we did not see any significant increase in out-of-plane proton conductivity (σ_{OP}) (Fig. S7). A similar observation was made for out-of-plane water and H_3O^+ ion self-diffusion coefficients (Fig. 7c and d). This could likely be explained by inspecting back the orientation of Nafion chains next to the substrate (simulation, Fig. 4a and b). MD simulations showed that Cys promotes a surface-parallel orientation of Nafion backbones near the substrate. This alignment arranges the $-SO_3H$ groups parallel to the surface (Fig. 4b), creating lamellar, in-plane hydrophilic domains that facilitate lateral (in-plane) proton transport. However, such excessive surface-parallel ordering may have reduced vertical connectivity of ionic pathways and water channels, thereby limiting proton transport across ionomer films (σ_{OP}). Consistently, both out-of-plane proton conductivity and water/H_3O^+ diffusion coefficients showed no significant improvement.

What did we learn?

In summary, these observations pointed toward the fact that localized chain order can impact proton conductivity in a certain direction in ionomer films. When Nafion chains align more parallel to the substrate, in-plane proton conductivity improves. However, excessive surface-parallel orientation can compromise out-of-plane conductivity. Similar conclusions have been drawn by others,[36,89,90] where oriented surface-parallel lamellae of ionic block copolymers on electrodes enhanced in-plane ionic conductivity, but suppressed through-plane conductivity. In contrast, our earlier work demonstrated that engineering the electrode interface with spiderweb-like amino silanes disrupted surface-parallel lamellae, while inducing some chain order in the out-of-plane direction, resulting in a significant increase in out-of-plane proton conductivity.[10] In another relevant work, an ionomer having macrocyclic cavity-forming units and self-assembly capabilities created ellipsoidal features, where surface-parallel stacking of ionomer chains improved in-plane proton conductivity, while stacking of cavity-forming units perpendicular to the substrate enhanced out-of-plane proton conductivity.[1] These findings collectively demonstrate that improvement in proton conductivity in a certain direction has a lot to do with how the chains are packed and how the ion-conducting pathways are oriented. Therefore, strategic ionomer design, control over ionomer packing, and interfacial engineering can play a critical role in gaining control over ion-conduction pathways in electrochemical systems.

Our work draws attention to another intriguing observation. Birefringence (Δn) measurements,[10,25] surface enhanced FTIR,[32] Raman[40] spectroscopy, and simulations (both from previous studies[41] and this work showing chain distribution (Fig. 6c) and orientation (Fig. 4a and b)), indicate that on unmodified Au electrodes, Nafion chains or chain fragments tend to align parallel to the substrate, interacting directly with Au *via* Nafion's SO_3^- groups. In contrast, on Cys-modified Au, Nafion chains interact primarily with the terminal $-NH_2$ groups of Cys while remaining slightly lifted away from the substrate. Although Nafion chains experience interactions in both cases, the better in-plane proton conductivity observed on Cys-modified Au could be rationalized by a milder confinement effect exerted by Cys on the Nafion chains. Nafion chains anchored to Cys while hanging a bit up from the substrate experience less confinement and greater mobility compared to chains that are directly anchored to and lying on bare Au. Au, being a hard, non-penetrable wall-like substrate, totally blocks molecular mobility in one direction (*i.e.*, below Au surface); while Cys-anchored, hanging ionomer chains can still swing and sway and retain multi-directional mobility. Similar concepts are discussed in polymer physics as the impact of hard *vs.* soft confinement.[87,91] Preventing direct contact of ionomer chains with substrate and/or modulating ionomer-water localization across the ionomer film may thus allow greater chain freedom and rotational relaxation of water molecules, both critical for proton transport.

Conclusions

In this work, we demonstrated that modifying Au electrodes with cysteamine (Cys) significantly enhances the in-plane proton conductivity of Nafion thin films by alleviating the confinement imposed by direct ionomer–metal interfacial contact and interactions. The Cys modification created a thin, uniform monolayer that facilitated a more ordered, surface-parallel Nafion backbone orientation near the interface while allowing the chains to remain slightly elevated from the substrate, thereby reducing direct chain pinning to Au and likely enabling greater segmental mobility. The reduced interfacial confinement, critical for proton transport, was also supported by the reduced storage modulus of the Nafion films on Cys–Au as compared to on bare Au. MD simulations showed that this interfacial engineering increased the population of water and hydronium ions near the substrate and enhanced their self-diffusion coefficients, aligning with the experimentally observed 4-fold increase in in-plane conductivity (σ_{IP}). However, out-of-plane conductivity (σ_{OP}) remained almost

unchanged, as Nafion chains predominantly oriented parallel to the substrate, supporting in-plane proton transport rather than across the planes. Overall, this study highlights that interfacial design using tailored linkers, like Cys, can effectively mitigate confinement effects in ionomer thin films and improve proton transport in targeted directions. Our future work will focus on systematic exploration of linker chemistry and architecture to simultaneously optimize in-plane and out-of-plane ion conduction pathways, thereby advancing electrochemical device performance.

Conflicts of interest

The authors declare no conflict of interest.

Data availability

All data supporting the findings of this study are provided in the article and its supplementary information (SI). Supplementary information: QCM, AFM, out-of-plane EIS measurements, and simulation data. See DOI: https://doi.org/10.1039/d5lp00245a.

Acknowledgements

The research was primarily supported by the National Science Foundation (NSF) CAREER Award (NSF-DMR #1750040) and NSF-DMR# 2520078. The authors also acknowledge partial support through the U.S. Department of Energy (DOE), Office of Science, Basic Energy Sciences (BES) Early CAREER Award (#DE-SC0020336), and NSF-CBET#2310185. K. A. C. thanks the Fulbright Scholars Program and the University of Nebraska Collaboration Initiative Grant for their support. R. K. and G. A. acknowledge support from the NSF (#1845795). Part of this research (XPS, birefringence, AFM) was performed in the Nebraska Nanoscale Facility: National Nanotechnology Coordinated Infrastructure and the Nebraska Center for Materials and Nanoscience, which are supported by the NSF under Award ECCS: 2025298, and the Nebraska Research Initiative. The authors also acknowledge the Nano-Engineering Research Core Facility (NERCF) at UNL, which is partially funded by the Nebraska Research Initiative, for SEM-EDX and CR-AFM studies. K. A. C. and O. A. O acknowledge Sourav Sutradhar for assistance in AFM imaging experiments. The simulations were conducted on LSU HPC facilities and the LONI HPC facilities.

References

1 S. Chatterjee, E. Zamani, S. Farzin, I. Evazzade, O. A. Obewhere, T. Johnson, *et al.*, Molecular-Level Control Over Ionic Conduction and Ionic Current Direction by Designing Macrocycle-based Ionomers, *JACS Au*, 2022, **2**, 1144–1159.
2 S. Farzin, E. Zamani and S. K. Dishari, Unraveling Depth-Specific Ionic Conduction and Stiffness Behavior across Ionomer Thin Films and Bulk Membranes, *ACS Macro Lett.*, 2021, **10**, 791–798.
3 A. Kusoglu and A. Z. Weber, New Insights into Perfluorinated Sulfonic-Acid Ionomers, *Chem. Rev.*, 2017, **117**, 987–1104.
4 M. A. Modestino, D. K. Paul, S. Dishari, S. A. Petrina, F. I. Allen, M. A. Hickner, *et al.*, Self-assembly and transport limitations in confined Nafion films, *Macromolecules*, 2013, **46**, 867–873.
5 S. K. Dishari and M. A. Hickner, Antiplasticization and water uptake of Nafion® thin films, *ACS Macro Lett.*, 2012, **1**, 291–295.
6 S. K. Dishari and M. A. Hickner, Confinement and proton transfer in nafion thin films, *Macromolecules*, 2013, **46**, 413–421.
7 B. Frank and A. P. Gast, Polymer mobility in thin films, *Macromolecules*, 1996, **29**, 6531–6534.
8 S. K. Dishari, Current understanding of proton conduction in confined ionomeric systems, *J. Postdoc. Res.*, 2014, **2**, 30–39.
9 O. A. Obewhere, K. Acurio-Cerda, S. Sutradhar, M. Dike, R. Keloth and S. K. Dishari, Unravel-engineer-design: a three-pronged approach to advance ionomer performance at interfaces in proton exchange membrane fuel cells, *Chem. Commun.*, 2024, **60**, 13114–13142.
10 O. A. Obewhere and S. K. Dishari, Engineering Ionomer-Substrate Interface to Improve Thin-Film Proton Conductivity in Proton Exchange Membrane Fuel Cells, *ACS Appl. Polym. Mater.*, 2024, **6**, 4535–4546.
11 S. Farzin, A. Sarella, M. A. Yandrasits and S. K. Dishari, Fluorocarbon-Based Ionomers with Single Acid and Multiacid Side Chains at Nanothin Interfaces, *J. Phys. Chem. C*, 2019, **123**, 30871–30884.
12 M. Tesfaye, A. N. MacDonald, P. J. Dudenas, A. Kusoglu and A. Z. Weber, Exploring substrate/ionomer interaction under oxidizing and reducing environments, *Electrochem. Commun.*, 2018, **87**, 86–90.
13 Y. Ono and Y. Nagao, Interfacial Structure and Proton Conductivity of Nafion at the Pt-Deposited Surface, *Langmuir*, 2016, **32**, 352–358.
14 A. Ohira, S. Kuroda, H. F. M. Mohamed and B. Tavernier, Effect of interface on surface morphology and proton conduction of polymer electrolyte thin films, *Phys. Chem. Chem. Phys.*, 2013, **15**, 11494–11500.
15 T. Kawamoto, M. Aoki, T. Kimura, P. Chinapang, T. Mizusawa, N. L. Yamada, *et al.*, Sublayered Structures of Hydrated Nafion® Thin Film Formed by Casting on Pt Substrate Analyzed by X-ray Absorption Spectroscopy under Ambient Conditions and Neutron Reflectometry at Temperature of 80 °C and Relative Humidity of 30–80%, *Electrochemistry*, 2019, **87**, 270–275.
16 S. Poojary, M. N. Islam, U. N. Shrivastava, E. P. L. Roberts and K. Karan, Transport and electrochemical interface pro-

perties of ionomers in low-pt loading catalyst layers: Effect of ionomer equivalent weight and relative humidity, *Molecules*, 2020, **25**, 1–14.
17 W. Y. Hsu and T. D. Gierke, Ion transport and clustering in nafion perfluorinated membranes, *J. Membr. Sci.*, 1983, **13**, 307–326.
18 H. Haubold, T. Vad, H. Jungbluth and P. Hiller, Nano structure of NAFION : a SAXS study, *Electrochim. Acta*, 2001, **46**, 1559–1563.
19 K. Schmidt-rohr and Q. Chen, Parallel cylindrical water nanochannels in Nafion fuel-cell membranes, *Nat. Mater.*, 2008, **7**, 75–83.
20 B. Loppinet and G. Gebel, Rodlike Colloidal Structure of Short Pendant Chain Perfluorinated Ionomer Solutions, *Langmuir*, 1998, **14**, 1977–1983.
21 J. A. Elliott, J. A. Elliott, D. Wu, J. Paddison and R. B. Moore, A unified morphological description of Nafion membranes from SAXS and mesoscale simulations, *Soft Matter*, 2011, **7**, 6729–7124.
22 A. Kusoglu, T. J. Dursch and A. Z. Weber, Nanostructure/Swelling Relationships of Bulk and Thin-Film PFSA Ionomers, *Adv. Funct. Mater.*, 2016, **26**, 4961–4975.
23 K. D. Kreuer and G. Portale, A critical revision of the nanomorphology of proton conducting ionomers and polyelectrolytes for fuel cell applications, *Adv. Funct. Mater.*, 2013, **23**, 5390–5397.
24 A. Kusoglu, D. Kushner, D. K. Paul, K. Karan, M. A. Hickner and A. Z. Weber, Impact of substrate and processing on confinement of nafion thin films, *Adv. Funct. Mater.*, 2014, **24**, 4763–4774.
25 D. I. Kushner, A. Kusoglu, N. J. Podraza and M. A. Hickner, Substrate-Dependent Molecular and Nanostructural Orientation of Nafion Thin Films, *Adv. Funct. Mater.*, 2019, **29**, 1–10.
26 I. Yagi, K. Inokuma, K. Kimijima and H. Notsu, Molecular Structure of Buried Perfluorosulfonated Ionomer/Pt Interface Probed by Vibrational Sum Frequency Generation Spectroscopy, *J. Phys. Chem. C*, 2014, **118**, 26182–26190.
27 D. L. W. Iii, J. Chlistunoff, J. Majewski and R. L. Borup, Nafion Structural Phenomena at Platinum and Carbon Interfaces, *J. Am. Chem. Soc.*, 2009, **131**, 18096–18104.
28 J. L. Keddie, R. A. L. Jones and R. A. Cory, Interface and Surface Effects on the Glass-transition Temperature in Thin Polymer Films, *Faraday Discuss.*, 1994, **98**, 219–230.
29 A. Kusoglu, Ionomer Thin Films in PEM Fuel Cells, in *Fuel Cells and Hydrogen Production*, ed. T.E Lipman and A.Z Weber, Springer, 2019, pp. 417–438.
30 M. Bass, A. Berman, A. Singh, O. Konovalov and V. Freger, Surface-Induced Micelle Orientation in Nafion Films, *Macromolecules*, 2011, **44**, 2893–2899.
31 D. K. Paul, K. Karan, A. Docoslis, J. B. Giorgi and J. Pearce, Characteristics of self-assembled ultrathin Nafion films, *Macromolecules*, 2013, **46**, 3461–3475.
32 T. J. Zimudzi and M. A. Hickner, Signal Enhanced FTIR Analysis of Alignment in NAFION Thin Films at SiO_2 and Au Interfaces, *ACS Macro Lett.*, 2016, **5**, 83–87.
33 A. Chowdhury, A. Bird, J. Liu, I. V. Zenyuk, A. Kusoglu, C. J. Radke, *et al.*, Linking Perfluorosulfonic Acid Ionomer Chemistry and High-Current Density Performance in Fuel-Cell Electrodes, *ACS Appl. Mater. Interfaces*, 2021, **13**, 42579–42589.
34 J. A. Dura, V. S. Murthi, M. Hartman, S. K. Satija and C. F. Majkrzak, Multilamellar interface structures in Nafion, *Macromolecules*, 2009, **42**, 4769–4774.
35 S. C. DeCaluwe, P. A. Kienzle, P. Bhargava, A. M. Baker and J. A. Dura, Phase segregation of sulfonate groups in Nafion interface lamellae, quantified via neutron reflectometry fitting techniques for multi-layered structures, *Soft Matter*, 2014, **10**, 5763–5776.
36 Y. Ogata, T. Abe, S. Yonemori, N. L. Yamada, D. Kawaguchi and K. Tanaka, Impact of the Solid Interface on Proton Conductivity in Nafion Thin Films, *Langmuir*, 2018, **34**, 15483–15489.
37 S. Ott, F. Du, M. L. Luna, T. A. Dao, B. R. Cuenya, A. Orfanidi, *et al.*, Understanding the Performance Increase of Catalysts Supported on N-Functionalized Carbon in PEMFC Catalyst Layers, *J. Electrochem. Soc.*, 2022, **169**, 1–14.
38 S. K. Dishari, C. A. Rumble, M. Maroncelli, J. A. Dura and M. A. Hickner, Unraveling the Complex Hydration Behavior of Ionomers under Thin Film Confinement, *J. Phys. Chem. C*, 2018, **122**, 3471–3481.
39 C. Zhang, M. Davies and K. Karan, Probing interfacial interactions of nafion ionomer: Thermal expansion of nafion thin films on substrates of different hydrophilicity/hydrophobicity, *J. Polym. Sci., Part B: Polym. Phys.*, 2019, **57**, 343–352.
40 J. Zeng, D. i. Jean, C. Ji and S. Zou, In Situ Surface-Enhanced Raman Spectroscopic Studies of Nafion Adsorption on Au and Pt Electrodes, *Langmuir*, 2012, **28**, 957–964.
41 I. Kendrick, D. Kumari, A. Yakaboski, N. Dimakis and E. S. Smotkin, Elucidating the ionomer-electrified metal interface, *J. Am. Chem. Soc.*, 2010, **132**, 17611–17616.
42 T. Masuda, F. Sonsudin, P. R. Singh, H. Naohara and K. Uosaki, Potential-dependent adsorption and desorption of perfluorosulfonated ionomer on a platinum electrode surface probed by electrochemical quartz crystal microbalance and atomic force microscopy, *J. Phys. Chem. C*, 2013, **117**, 15704–15709.
43 S. Jiang, Q. Xiang, Z. Xie, N. Yang, J. Liu, L. Li, *et al.*, Influence of the Pt/ionomer/water interface on the oxygen reduction reaction: insights into the micro-three-phase interface, *Chem. Sci.*, 2024, **15**, 19290–19298.
44 J. Tymoczko, F. Calle-Vallejo, V. Colic, M. T. M. Koper, W. Schuhmann and A. S. Bandarenka, Oxygen reduction at a Cu-modified Pt(111) model electrocatalyst in contact with nafion polymer, *ACS Catal.*, 2014, **4**, 3772–3778.
45 Z. Xu, S. Yuan, L. An, S. Shen, Q. Xu, X. Yan, *et al.*, Effect of Substrate Surface Charges on Proton Conduction of Ultrathin Nafion Films, *ACS Appl. Mater. Interfaces*, 2023, **15**, 10735–10743.

46 A. Kumar, E. J. Park, Y. S. Kim and J. S. Spendelow, Surface Functionalization of Carbon Black for PEM Fuel Cell Electrodes, *Macromol. Chem. Phys.*, 2024, **225**, 1–27.
47 M. A. Modestino, A. Kusoglu, A. Hexemer, A. Z. Weber and R. A. Segalman, Controlling Nafion Structure and Properties via Wetting Interactions, *Macromolecules*, 2012, **45**, 4681–4688.
48 G. Doo, S. Yuk, J. H. Lee, S. Choi, D. H. Lee, D. W. Lee, *et al.*, Nano-scale control of the ionomer distribution by molecular masking of the Pt surface in PEMFCs, *J. Mater. Chem. A*, 2020, **8**, 13004–13013.
49 Y. Li, J. Hart, L. Profitt, S. Intikhab, S. Chatterjee, M. Taheri, *et al.*, Sequential Capacitive Deposition of Ionic Liquids for Conformal Thin Film Coatings on Oxygen Reduction Reaction Electrocatalysts, *ACS Catal.*, 2019, **9**, 9311–9316.
50 R. Friedmann and T. Van Nguyen, Optimization of the Microstructure of the Cathode Catalyst Layer of a PEMFC for Two-Phase Flow, *J. Electrochem. Soc.*, 2010, **157**, 1–7.
51 R. P. Dowd, C. S. Day and T. Van Nguyen, Engineering the Ionic Polymer Phase Surface Properties of a PEM Fuel Cell Catalyst Layer, *J. Electrochem. Soc.*, 2017, **164**, F138–F146.
52 Y. Yang, C. Zhao, Z. Wang, X. Fan and C. Yan, Synergistic effects of N-doping and mesoporous structures in block copolymer-derived three-dimensionally ordered mesoporous carbon for PEMFC, *Int. J. Hydrogen Energy*, 2024, **51**, 747–757.
53 Y. Li, S. Intikhab, A. Malkani, B. Xu and J. Snyder, Ionic Liquid Additives for the Mitigation of Nafion Specific Adsorption on Platinum, *ACS Catal.*, 2020, **10**, 7691–7698.
54 G. R. Zhang, T. Wolker, D. J. S. Sandbeck, M. Munoz, K. J. J. Mayrhofer, S. Cherevko, *et al.*, Tuning the Electrocatalytic Performance of Ionic Liquid Modified Pt Catalysts for the Oxygen Reduction Reaction via Cationic Chain Engineering, *ACS Catal.*, 2018, **8**, 8244–8254.
55 A. Avid, J. L. Ochoa, Y. Huang, Y. Liu, P. Atanassov and I. V. Zenyuk, Revealing the role of ionic liquids in promoting fuel cell catalysts reactivity and durability, *Nat. Commun.*, 2022, **13**, 1–13.
56 K. Brunnengräber, K. Jeschonek, M. George, G. r. Zhang and B. J. M. Etzold, Ionic Liquid Modified Electrocatalysts : a STEM-EDX Approach for Identification of Local Distributions within Ionomer Containing Catalysts Layers, *Chem.: Methods*, 2023, 1–9.
57 Y. Li, T. V. Cleve, R. Sun, R. Gawas, G. Wang, M. Tang, *et al.*, Modifying the Electrocatalyst – Ionomer Interface via Sulfonated Poly(ionic liquid) Block Copolymers to Enable High- Performance Polymer Electrolyte Fuel Cells, *ACS Energy Lett.*, 2020, **5**, 1726–1731.
58 R. Sun, M. Agrawal, K. C. Neyerlin, J. D. Snyder and Y. A. Elabd, Proton Conducting Sulfonated Poly(Ionic Liquid) Block Copolymers, *Macromolecules*, 2022, **55**, 6716–6729.
59 R. Gawas, R. Sun, Y. Li, K. C. Neyerlin, Y. A. Elabd, M. Tang, *et al.*, Characterization of a Sulfonated Poly(Ionic Liquid) Block Copolymer as an Ionomer for Proton Exchange Membrane Fuel Cells using Rotating Disk Electrode, *J. Electrochem. Soc.*, 2021, **168**, 1–8.
60 S. Chatterjee, O. A. Obewhere, E. Zamani, R. Keloth, S. Farzin, M. D. Morton, *et al.*, Advancing ionomer design to boost interfacial and thin-film proton conductivity via styrene-calix[4]arene-based ionomers, *Cell Rep. Phys. Sci.*, 2023, **4**, 1–20.
61 K. Acurio Cerda, M. Kathol, G. Purohit, E. Zamani, M. D. Morton, O. Khalimonchuk, *et al.*, Cationic Lignin as an Efficient and Biorenewable Antimicrobial Material, *ACS Sustainable Chem. Eng.*, 2023, **11**, 10364–10379.
62 N. Pramounmat, C. N. Loney, C. Kim, L. Wiles, K. E. Ayers, A. Kusoglu, *et al.*, Controlling the Distribution of Perfluorinated Sulfonic Acid Ionomer with Elastin-like Polypeptide, *ACS Appl. Mater. Interfaces*, 2019, **11**, 43649–43658.
63 Z. Su, S. Kole, L. C. Harden, V. M. Palakkal, C. Kim, G. Nair, *et al.*, Peptide-Modified Electrode Surfaces for promoting Anion Exchange Ionomer Microphase Separation and Ionic Conductivity, *ACS Mater. Lett.*, 2019, **1**, 467–475.
64 Z. Su, N. Pramounmat, S. T. Watson and J. N. Renner, Engineered interaction between short elastin-like peptides and perfluorinated sulfonic-acid ionomer, *Soft Matter*, 2018, **14**, 3528–3535.
65 J. Snyder, T. Fujita, M. W. Chen and J. Erlebacher, Oxygen reduction in nanoporous metal-ionic liquid composite electrocatalysts, *Nat. Mater.*, 2010, **9**, 904–907.
66 Z. Li, S. C. Chang and R. S. Williams, Self-assembly of alkanethiol molecules onto platinum and platinum oxide surfaces, *Langmuir*, 2003, **19**, 6744–6749.
67 D. Y. Petrovykh, H. Kimura-Suda, A. Opdahl, L. J. Richter, M. J. Tarlov and L. J. Whitman, Alkanethiols on platinum: Multicomponent self-assembled monolayers, *Langmuir*, 2006, **22**, 2578–2587.
68 J. C. Love, L. A. Estroff, J. K. Kriebel, R. G. Nuzzo and G. M. Whitesides, Self-assembled monolayers of thiolates on metals as a form of nanotechnology, *Chem. Rev.*, 2005, **105**, 1103–1169.
69 M. Roushani, A. Valipour and M. Valipour, Layer-by-layer assembly of gold nanoparticles and cysteamine on gold electrode for immunosensing of human chorionic gonadotropin at picogram levels, *Mater. Sci. Eng., C*, 2016, **61**, 344–350.
70 J. Spadavecchia, D. Movia, C. Moore, C. M. Maguire, H. Moustaoui, S. Casale, *et al.*, Targeted polyethylene glycol gold nanoparticles for the treatment of pancreatic cancer: From synthesis to proof-of-concept in vitro studies, *Int. J. Nanomed.*, 2016, **11**, 791–822.
71 J. Spadavecchia, J. Moreau, J. Hottin and M. Canva, New cysteamine based functionalization for biochip applications, *Sens. Actuators, B*, 2009, **143**, 139–143.
72 J. Politi, J. Spadavecchia, M. Iodice and L. de Stefano, Oligopeptide-heavy metal interaction monitoring by hybrid gold nanoparticle based assay, *Analyst*, 2015, **140**, 149–155.
73 D. K. Paul, R. McCreery and K. Karan, Proton Transport Property in Supported Nafion Nanothin Films by

Electrochemical Impedance Spectroscopy, *J. Electrochem.*, 2014, **161**, F1395–F1402.

74 S. Farzin, T. J. Johnson, S. Chatterjee, E. Zamani and S. K. Dishari, Ionomers From Kraft Lignin for Renewable Energy Applications, *Front. Chem.*, 2020, **8**, 1–17.

75 B. D. Vogt, E. K. Lin, W. l. Wu and C. C. White, Effect of film thickness on the validity of the Sauerbrey equation for hydrated polyelectrolyte films, *J. Phys. Chem. B*, 2004, **108**, 12685–12690.

76 S. A. Petrina, *Water Sorption, viscoelastic, and optical properties of thin Nafion films [Internet]*, 2013. Available from: https://etda.libraries.psu.edu/files/final_submissions/9040.

77 D. I. Kushner and M. A. Hickner, Water Sorption in Electron-Beam Evaporated SiO_2 on QCM Crystals and Its Influence on Polymer Thin Film Hydration Measurements, *Langmuir*, 2017, **33**, 5261–5268.

78 Y. Kobayashi, W. Zheng, T. B. Chang, K. Hirata, R. Suzuki, T. Ohdaira, *et al.*, Nanoporous structure of sputter-deposited silicon oxide films characterized by positronium annihilation spectroscopy, *J. Appl. Phys.*, 2002, **91**, 1704–1706.

79 H. K. (Key) Shim, D. K. Paul and K. Karan, Resolving the contradiction between anomalously high water uptake and low conductivity of nanothin Nafion films on SiO_2 substrate, *Macromolecules*, 2015, **48**, 8394–8397.

80 T. Kondo, M. Yanagida, K. Shimazu and K. Uosaki, Determination of thickness of a self-assembled monolayer of dodecanethiol on Au(111) by angle-resolved X-ray photoelectron spectroscopy, *Langmuir*, 1998, **14**, 5656–5658.

81 W. N. W. Shukri, N. Bidin, S. Islam, G. Krishnan, M. A. A. Bakar and M. S. Affandi, Synthesis and characterization of uncoated and cysteamine-coated nanoparticles by pulsed laser ablation, *J. Nanophotonics*, 2020, **10**, 046007.

82 M. Wirde, U. Gelius and L. Nyholm, Self-assembled monolayers of cystamine and cysteamine on gold studied by XPS and voltammetry, *Langmuir*, 1999, **15**, 6370–6378.

83 M. T. Lee, C. C. Hsueh, M. S. Freund and G. S. Ferguson, Air oxidation of self-assembled monolayers on polycrystalline gold: The role of the gold substrate, *Langmuir*, 1998, **14**, 6419–6423.

84 S. Y. Lee, J. Noh, E. Ito, H. Lee and M. Hara, Solvent effect on formation of cysteamine self-assembled monolayers on Au(111), *Jpn. J. Appl. Phys.*, 2003, **42**, 236–241.

85 R. M. Petoral Jr and K. Uvdal, Arg–Cys and Arg–cysteamine adsorbed on gold and the G-protein– adsorbate interaction, *Colloids Surf., B*, 2002, **25**, 335–346.

86 C. R. Randall, L. Zou, H. Wang, J. Hui, J. Rodríguez-López, M. Chen-Glasser, *et al.*, Morphology of Thin-Film Nafion on Carbon as an Analogue of Fuel Cell Catalyst Layers, *ACS Appl. Mater. Interfaces*, 2024, **16**, 3311–3324.

87 R. P. Sharma and P. F. Green, Role of "hard" and "soft" Confinement on Polymer Dynamics at the Nanoscale, *ACS Macro Lett.*, 2017, **6**, 908–914.

88 Y. Guo, C. Zhang, C. Lai, R. D. Priestley, M. D'Acunzi and G. Fytas, Structural relaxation of polymer nanospheres under soft and hard confinement: Isobaric versus isochoric conditions, *ACS Nano*, 2011, **5**, 5365–5373.

89 J. P. Coote, T. Kinsey, D. P. Street, S. M. Kilbey, J. R. Sangoro and G. E. Stein, Surface-Induced Ordering Depresses Through-Film Ionic Conductivity in Lamellar Block Copolymer Electrolytes, *ACS Macro Lett.*, 2020, **9**, 565–570.

90 J. P. Coote, S. K. J. Adotey, J. R. Sangoro and G. E. Stein, Interfacial Effects in Conductivity Measurements of Block Copolymer Electrolytes, *ACS Polym. Au*, 2023, **3**, 331–343.

91 S. J. Xie, H. J. Qian and Z. Y. Lu, Hard and soft confinement effects on the glass transition of polymers confined to nanopores, *Polymer*, 2015, **56**, 545–552.